Available online at www.sciencedirect.com

ScienceDirect

Ceramics International 40 (2014) 1575–1586

CERAMICS INTERNATIONAL

www.elsevier.com/locate/ceramint

Structural and microwave characterization of $Ni_{0.2}Co_xZn_{0.8-x}Fe_2O_4$ for antenna applications

Kumar Mohit[a], Vibha Rani Gupta[a], Nisha Gupta[a], S.K. Rout[b,*]

[a]Department of Electronics and Communication Engineering, Birla Institute of Technology, Mesra, Ranchi, 835215 Jharkhand, India
[b]Department of Applied Physics, Birla Institute of Technology, Mesra, Ranchi, 835215 Jharkhand, India

Received 31 May 2013; received in revised form 8 July 2013; accepted 9 July 2013
Available online 26 July 2013

Abstract

Nickel–cobalt–zinc ferrites, $Ni_{0.2}Co_xZn_{0.8-x}Fe_2O_4$ (with $x=0$, 0.2, 0.4, 0.6, 0.8,) have been prepared using the auto-combustion method. X-ray diffraction, Fourier transform infrared (FT-IR) and Raman spectroscopy confirmed the cubic spinel structure of the ferrites. Microwave dielectric constant (ε_r) and quality factor ($Q \times f$) were measured by using the Hakki–Coleman technique. Dielectric constant calculated using the Clausius–Mossoitti relation showed good agreement with the experimental value. Relative permeability of the ferrites was calculated by using the Nicholson–Ross–Weir conversion technique. Dielectric constant (ε_r) decreased from 7.474 to 5.548 and temperature coefficient of resonant frequency (τ_f) increased from -75.85 ppm/°C to -19.32 ppm/°C, respectively, and relative permeability increased from 2.1085 to 3.2179 with increase in Cobalt content. The composition $Ni_{0.2}Co_{0.2}Zn_{0.6}Fe_2O_4$ was used to develop ferrite resonator antennas (FRA) and was studied in cylindrical, triangular and cuboid shapes with co-axial probe feeding mechanisms. The antenna characteristics were simulated using high frequency structure simulation (HFSS) software and a good agreement has been achieved between the measured and simulated results. The cuboid shaped FRA show maximum bandwidth of 990 MHz, while the cylindrical shaped FRA show a maximum gain of 3.48 dB, respectively.

Keywords: Antenna; Magneto-dielectrics; Microwave properties

1. Introduction

Miniaturization of high frequency antennas while maintaining desirable bandwidth, impedance, and loss characteristics has recently attracted great attention [1]. As the mobile communication devices are smaller, antenna miniaturization is becoming increasingly important. A dielectric resonator antenna (DRA) is fabricated from low-loss microwave dielectric material, whose resonant frequency is predominantly a function of size, shape, and permittivity. However, as the permittivity increases, the efficiency and the frequency bandwidth of the antenna are reduced, leading to limitations in size reduction and trade off in performances. At this time, one of the solutions for the antenna-downsizing is using materials with permittivity and permeability greater than one. In recent years, many studies on miniaturization of the antenna using magneto-dielectric material have been reported [2–5]. The use of magneto-dielectric material offers an additional degree of freedom in order to improve the performance of antenna. Hence some characteristics of antenna can be improved to satisfy the requirement of applications by suitably tuning the material parameters [2].

Ferrites are technologically important materials that are used in the fabrication of magnetic, electronic and microwave devices. Ferrites with low loss tangents (both dielectric and magnetic) are very useful to the design of miniaturized antenna and also for maintaining the electrical dimensions (the electrical length is the product of the geometrical length of the medium and its refractive index) [6]. The performance of porous ferrite materials in their bulk form where the grain size is big leads to high magnetic loss [7]. This is due to their higher electrical conductivity and domain wall resonance [8–11]. So, obtaining microstructure with dense, uniform and small grain size is the key to obtain both low dielectric and magnetic losses making the candidate suitable to work at higher frequencies [12]. One way to achieve this, by synthesizing the

*Corresponding author. Tel.: +91 65 12 275 027.
E-mail addresses: skrout@bitmesra.ac.in, drskrout@gmail.com (S.K. Rout).

0272-8842/$ - see front matter © 2013 Elsevier Ltd and Techna Group S.r.l. All rights reserved.
http://dx.doi.org/10.1016/j.ceramint.2013.07.045

ferrite particles in nanometric scales before compacting them for sintering. When the size of the magnetic particle is smaller than the critical size for multi-domain formation, the particle is in a single domain state. Domain wall resonance is avoided, and the material can work at higher frequencies [7]. Several synthesize techniques have been reported to achieve ferrite nanoparticles [13–16]. Auto-combustion technique is one of the best techniques in terms of less energy consumption. Furthermore this technique has many other advantages like; the resultant product show better chemical homogeneity, higher reactivity, limited agglomeration which reduce the losses in the ceramics [17–20]. Also it has been reported that the magnetic properties can be improved compared to conventional ceramic method [21] as the use of nanoparticles sized material significantly enhances the densification and microwave dielectric properties [22,23].

Nickel–zinc ferrites are one of the most important soft ferrites whereby the high permeability and low power loss have become the most principal requirements for the electronic devices [24]. They have great potential as microwave materials on account of their high resistivity, ease of fabrication as well as low eddy current losses and high saturation magnetization as compared with other ferrites [25–30].Variation of the zinc concentration in these ferrites allows for tailoring the magnetic properties to suit the requirement of a particular application [31]. It is reported that the addition of cobalt reduces the magnetic losses and anisotropy, so that the material fit for the application at high frequency [32,33]. This paper present Co substituted Ni–Zn ferrite synthesized by auto-combustion route. Structural, dielectric and magnetic characteristics of Co substituted Ni–Zn ferrite nanoparticles have discussed and reports about their performances as an antenna.

2. Experimental procedure and core mathematics

2.1. Synthesis of Ni–Zn–Cu ferrite nanoparticles by auto-combustion reaction

High pure (99.99%, Merck India Chemicals) analytical grade reagents, Nickel nitrate, Zinc nitrate, Cobalt nitrate, Ferric nitrate and Citric acid were used for the synthesis of $Ni_{0.2}Co_xZn_{0.8-x}Fe_2O_4$ (NCZFO) nanoparticles. The stoichiometric proportions of the nitrate salts were taken for the preparation of NCZFO nanoparticles. A magnetic stirrer was used to mix an aqueous solution of the nitrate salts and citric acid with distilled water separately and then mixed together. After constant stirring for 2 h of this mixture solution at room temperature in ambient atmosphere, a precursor solution was formed. The molar ratio of nitrate solution to citric acid was kept at 1:1. A Small amount of ammonia hexahydrate solution was added into the precursor solution till the pH reaches a factor of 7. The precursor of the complexes metal ions was heated at 70 °C for 20 h to obtain the gel. Further heating of the gel (at approximately 100 °C) gives auto-combustion, which produces loose powder of the NCZFO [34]. The NCZFO powders were calcined at 500 °C for 4 h and used for further study.

2.2. Structural and micro-structural characterizations

The phase identification, crystallite size and lattice parameters of ferrite samples were analyzed using X-ray diffraction (Bruker D8-advance X-Ray Diffractometer) with Cu K_α radiation. The crystallite size was calculated from peak broadening using Scherrer formula,

$$D_{hkl} = \frac{0.9\,\lambda}{\beta \cos\,\theta} \tag{1}$$

where D_{hkl} is the crystallite size perpendicular to ($h\,k\,l$) plane, λ is the wavelength of X-ray used, β (rad.) is the FWHM of the diffraction peak and θ is the peak position. The X-ray density (ρ_x) of the samples was calculated using the relation given by Smit and Wijn [33,35]:

$$\rho_x = nM/N_A a^3 \tag{2}$$

where M is the molecular weight of the samples, N_A is the Avogadro's number, n is the number of formula unit present in a unit cell (in the present case, n=8) and a is the lattice parameter. X-ray density (ρ_x) was calculated using Eq. (2) and found to be in the range of 6.298–5.94 8g/cm^3. Structural changes were studied using Fourier transform infrared spectroscopy (FTIR) (IR-Prestige-21). Raman studies were performed using a spectrometer (Jobin-Yvon T64000 Spectrometer) with an excitation wavelength of 514.5 nm, from an Ar laser. The monophasic powder samples were granulated with polyvinyl alcohol as binder and were uniaxially pressed at a pressure of 6 t/cm^2 using steel dies of different geometry (cylindrical, rectangular and triangular). Sintering was performed in air environment in the temperature at 1200 °C for 4 h to obtain the bulk density to about 90% of their respective X-ray density. Water immersion technique was used to calculate the bulk density and apparent porosity of the sintered samples. The grain size and grain morphology of the sintered NCZFO were studied using scanning electron microscopy (SEM) on a Zeiss DSM 982 Gemini instrument with a Schottky emitter at an accelerating voltage of 2 kV and a beam current of 1 μA.

2.3. Microwave dielectric constant measurement

A Vector Network Analyzer (N5230A Agilent Technologies, USA) was used to perform microwave dielectric measurements in the $TE_{01\delta}$ mode for the cylindrical shaped NCZFO using the Hakki–Coleman [36] dielectric resonator method as modified and improved by Courtney [37]. In the $TE_{01\delta}$ mode, the field confinement is not complete in the z-direction and hence TE_{011} mode is designated as $TE_{01\delta}$. This mode is widely used in materials property characterization because in this mode there is no current crossing the dielectric and the conducting plates, so possible air gaps between the dielectric and the conducting plates have no effects on resonance properties of this mode [38]. The theoretical model is properly described for the configuration mentioned by Courtney and as modified from Kobayashi and Tanaka [39]. The $TE_{01\delta}$ resonance mode has been found most suitable for the real part of the relative dielectric constant (ε_r), and

a gain/loss factor (tan δ) of the specimen. These were obtained from the measured resonance frequency (f_r) and unloaded quality factor (Q_0) for the $TE_{01\delta}$ resonance mode [40,41].

The relative dielectric constant and loss factors were calculated from the following formulas [38]:

$$\varepsilon_r = 1 + \left(\frac{c}{\pi D f_r}\right)(\alpha^2 + \beta^2) \tag{3}$$

where c is the velocity of light, α is given by the mode chart [42] β is obtained from the resonance frequency (f_r) and the sample dimension. The tan δ is given by Hakki–Coleman [36] as described in Eq. (4):

$$\tan\ \delta = \frac{A}{Q_u} - BR_s \tag{4}$$

Here

$$A = 1 + \frac{W}{r} \tag{5}$$

$$B = \left(\frac{l\lambda}{2L}\right)^3 \frac{1+W}{30\pi_r^2 l} \tag{6}$$

$$W = \frac{J_1^2(\alpha_1)}{K_1^2(\beta_1)} \cdot \frac{K_0(\beta_1)K_2(\beta_1) - K_1^2(\beta_1)}{J_1^2(\alpha_1) - J_0(\alpha_1)J_2(\alpha_1)} \tag{7}$$

$$R_s = \sqrt{\frac{\pi f_r \mu}{\sigma}} \tag{8}$$

The function W is the ratio of electric field energy stored on the outside of the rod to the energy inside the rod. The λ is the free-space wavelength, L is the length of the dielectric specimen and l=an integer (1, 2, 3, 4…..). The σ is the conductivity of the shorting plate, and Q_0 is the unloaded quality factor of the dielectric resonator. If the dielectric material is isotropic then the characteristic equation for such a resonance structure for the TE_{011} mode is given by Eq. (9):

$$\alpha \frac{J_0(\alpha)}{J_1(\alpha)} = -\beta \frac{K_0(\beta)}{K_1(\beta)} \tag{9}$$

where $J_0(\alpha)$ and $J_1(\alpha)$ are the Bessel functions of the first kind of order zero and one, respectively. $K_0(\beta)$ and $K_1(\beta)$ are the modified Bessel functions of the second kind of orders zero and one, respectively.

Kobayashi and Katoh [43] described a method for the experimental determination of R_s which employs two rod samples cut from the same dielectric rod with equal diameters but different lengths. The rod for a TE_{01l} resonator is "l" times as long as the other rod for a TE_{011} resonator, where $l \geq 2$ Here subscripts l and 1 are denoted as quantities for both resonators, respectively. Because of the different conduction loss contributions in the two cases, the modes have almost the same resonance frequency but differ in unloaded Q; i.e if $f_{0l} = f_{01}$, then $Q_{0l} > Q_{01}$. Because both rods have the same (tan δ), the expression for (R_s) is given by Eq. (10) [39]:

$$R_s = 30\pi^2 \left(\frac{2L}{l\lambda}\right)^3 \cdot \frac{r+W}{1+W} \cdot \frac{l}{l-1} \cdot \left(\frac{1}{Q_{01}} - \frac{1}{Q_{0l}}\right) \tag{10}$$

Then substitution of Eq. (10) into Eq. (4) yields:

$$\tan\ \delta = \frac{A}{l-1}\left(\frac{1}{Q_{0l}} - \frac{1}{Q_{01}}\right) \tag{11}$$

This calculation facilitates the precise measurement of (tan δ). A schematic diagram of the experimental setup is shown in Fig. 1.

The quality factor ($Q \times f$) was measured using a reflection mode gold-coated copper cavity [41].

The τ_f value of samples has been measured by introducing the cavity in temperature controlled chamber. The following equation has been used for this:

$$\tau_f = \left(\frac{1}{f}\right)\left(\frac{\Delta f}{\Delta T}\right) \tag{12}$$

2.4. Calculation of microwave magnetic constant

The Nicholson–Ross–Weir conversion technique was used to calculate the microwave permeability by determining the S-parameters using the Vector Network Analyzer in a TM_{010} resonance mode. This method provides a direct calculation of both the permittivity and permeability from the S-parameters [44].

It is the most commonly used method for performing such conversion. Measurement of reflection coefficient and transmission coefficient requires all four (S_{11}, S_{21}, S_{12}, S_{22}) or a pair (S_{11}, S_{21}) of S-parameters of the material under test to be measured. The present calculation for permeability includes only S_{11} and S_{21} parameter as under.

The transmission and reflection co-efficient are related to S-parameter as per following formula [44,45]:

$$T = \frac{S_{11} + S_{21} - \Gamma}{1 - (S_{11} + S_{21})\Gamma} \tag{13}$$

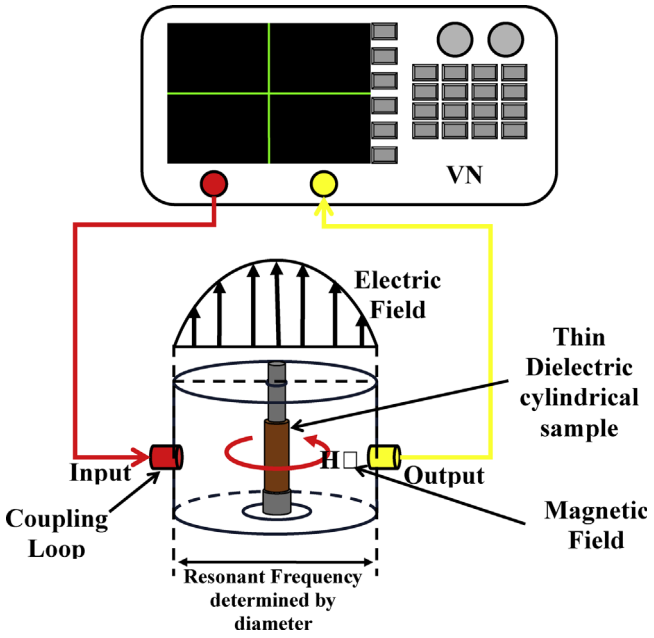

Fig. 1. Measurement of resonant frequency and S-parameter using cavity resonator.

$$\Gamma = X \pm \sqrt{X^2-1} \tag{14}$$

where

$$X = \frac{S_{11}^2 - S_{21}^2 + 1}{2S_{11}} \tag{15}$$

Here, Γ is reflection co-efficient; T is transmission co-efficient, S_{11} and $S_{21}$are reflection loss and insertion loss, respectively.

The free space wavelength (λ_0), cut-off wave length (λ) are related with transmission coefficient and diameter of cylindrical shaped sample as (16);

$$\frac{1}{2} = \left(\frac{\varepsilon_r \mu_r}{\lambda_0^2} - \frac{1}{\lambda_c^2}\right) = -\left(\frac{1}{2\pi L}\ln\left(\frac{1}{T}\right)\right)^2 \tag{16}$$

The permeability could be calculated by using formula:

$$\mu_r = \frac{1+\Gamma}{(1-\Gamma)\sqrt{(1/\lambda_0^2) - (1/\lambda_c^2)}} \tag{17}$$

By substitute Eq. (16) in Eq. (17), we got a quadratic Eq. in terms of permeability (μ_r),

$$(1+\Gamma^2-2\Gamma)\left(\frac{1}{\lambda_0^2} - \frac{1}{\lambda_c^2}\right)\mu_r{}^2 - \left((1+\Gamma^2+2\Gamma)\frac{\varepsilon_r}{\lambda_0^2}\right)\mu_r + (1+\Gamma^2+2\Gamma)\frac{1}{\lambda_c^2} = 0 \tag{18}$$

The permeability of the NCZFO samples was calculated by solving the above equation.

2.5. Ferrite resonator antenna (FRA) measurements

The resonator antenna behavior was studied by using sintered $Ni_{0.2}Co_{0.2}Zn_{0.2}Fe_2O_4$ ceramics in cylindrical, cuboid and triangular shapes. The schematic diagram of the FRA is given in the Fig. 2.

The ferrite resonators were excited by coaxial cable. The FRA is placed above a conducting ground plane made of FR4 sheet with copper coating on both side. The outer conductor of a subminiature version A (SMA) connector is connected to the ground plane and the inner conductor (probe) is connected to the Ferrite resonator (FR). The probe is located at $x=6.7$ mm and $\varphi=0^\circ$ as shown in Fig. 2. The fixed dimension of ground plane ($L \times W \times T = 100$ mm $\times$ 100 mm $\times$ 1.6 mm) and coaxial probe of different length were used for different shaped FRA. The probe lengths are optimized to obtain proper impedance matching with respect to the $Ni_{0.2}Co_{0.2}Zn_{0.6}Fe_2O_4$ composition, for each geometry of FRA. However, this impedance matching could also be adjusted by changing the probe length with respect to the other compositions. The composition $Ni_{0.2}Co_{0.2}Zn_{0.6}Fe_2O_4$ is chosen as a representative (for briefness only) one due to its lowest quality factor (highest dielectric loss) and highest magnetic loss among the Co containing compositions. It is known that lower the quality factor higher the bandwidth. Hence it is expected that the $Ni_{0.2}Co_{0.2}Zn_{0.6}Fe_2O_4$ composition will have the highest bandwidth but other compositions may show improved gain.

A detail of the measurement of resonant frequency for three different shaped (cylindrical, cuboid and triangular) FRA is as under.

In case of cylindrical FRA, the probe adjacent to the FRA can excite the basic mode, $HE_{11\delta}$ mode [40], whose resonant frequency f_r can be approximated by [46,47]

$$f_r = \frac{2.997 \times 10^8}{2\pi\sqrt{\varepsilon_r \mu_r}}\sqrt{\left(\frac{1.841}{r}\right)^2 + \left(\frac{\pi}{2h}\right)^2} \tag{19}$$

where μ_r is real part of permeability, ε_r is real part of permittivity. The cylindrical FRA under consideration has the height, h=7.2 mm, and radius, r=6.7 mm. The Eq. (19) is obtained with the hypothesis that the lateral and upper surface of the ferrite resonator is perfectly magnetic conductor (PMC). Because this assumption is verified only for infinite permittivity, it is only an approximation that leads to some 10% errors [48].

A comparison of the values from above equation to the following closed form of expression for the $HE_{11\delta}$ resonance frequency published in Ref. [49]:

$$f_r = \frac{6.324c}{2\pi r\sqrt{2+\varepsilon_r \mu_r}}\left(0.27 + 0.36\frac{r}{2h} + 0.02\left(\frac{r}{2h}\right)^2\right) \tag{20}$$

where the f_r is given in GHz and c is velocity of light. It is observed that there is variation in simulation and measured results and depends on the probe. This problem finds its origin

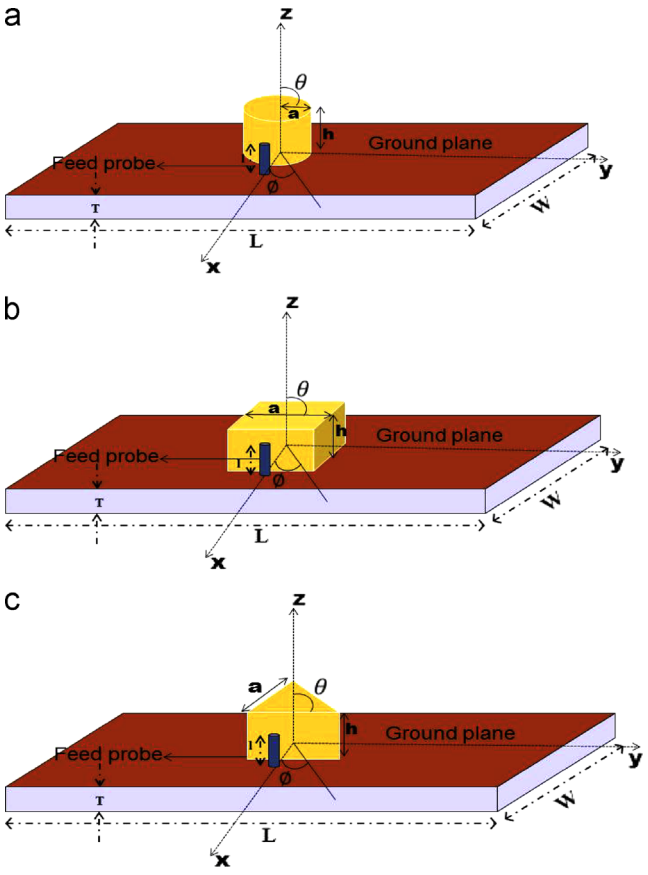

Fig. 2. The schematic representation of: (a) cylindrical, (b) cuboid and (c) triangular shaped FRA.

in the air gap between the DR and metallic conductors and has been thoroughly studied by Junker et al. [50,51].

In case of cuboid shape the probe adjacent to FRA excite the basic mode, TE^{Y}_{111} mode, whose resonant frequency f_r can be approximated by [52,53]:

$$f_r = \frac{k_0 c}{2\pi} \tag{21}$$

where $k_x^2 + k_y^2 + k_z^2 = k_0^2 \varepsilon_r \mu_r$, and k_x, k_y, k_z are given by

$$k_x = \frac{\pi}{a}, \quad k_z = \frac{\pi}{2h} \tag{22}$$

and

$$k_y \tan\left(\frac{k_y b}{2}\right) = \sqrt{(k_x^2 + k_z^2 - k_0^2)} \tag{23}$$

where k_x, k_y, k_z represent the mode wave numbers inside the dielectric resonator and k_0 is the free-space wave number. Cuboid shaped FRA under consideration has the length, a=9.7 mm, width, b=12.5 and height, h=7 mm.

In case of an equilateral-triangular FRA, resonance frequency of the excited mode TM_{mnl} is approximately given by [54,55]

$$f_r = \frac{c}{\sqrt{\varepsilon_r \mu_r}} \left[\left(\frac{4}{3a}\right)^2 (m^2 + n^2 + mn) + \left(\frac{1}{2h}\right)^2 \right] \tag{24}$$

where a is the length of each side of the triangle and h is the height of the resonator. The indices m, n and l should satisfy the condition l+m+n=0 but they all cannot be zero simultaneously. For low profile resonators where $a \gg h$, this expression can be further simplified as

$$f_r = \frac{c}{4h\sqrt{\varepsilon_r \mu_r}} \tag{25}$$

The designed triangular FRA has the height, h=7.5 mm and side, a=9.9 mm. The impedance bandwidth (return loss < -10 dB) were measured for all FRA using the relation [56].

$$\text{BW}\ (\%) = \left(\frac{OR}{CF}\right) \times 100 \tag{26}$$

Where, BW is the bandwidth, *OR* is the operating range and *CF* is the center frequency. All the simulation have done by using the HFSS software, which is based on Finite Element method.

3. Results and discussion

3.1. XRD patterns analysis

X-ray diffraction patterns of the NCZFO powder samples consist of seven diffraction lines of characteristic (2 2 0), (3 1 1), (2 2 2), (4 0 0), (4 2 2), (5 1 1) and (4 4 0) planes which indicate the single phase cubic spinal crystal structure with space group of $Fd\bar{3}m$, shown in Fig. 3. The sharp and intense peaks show the crystalline nature of the samples. The lattice parameter of NCZFO ferrites is determined by using the

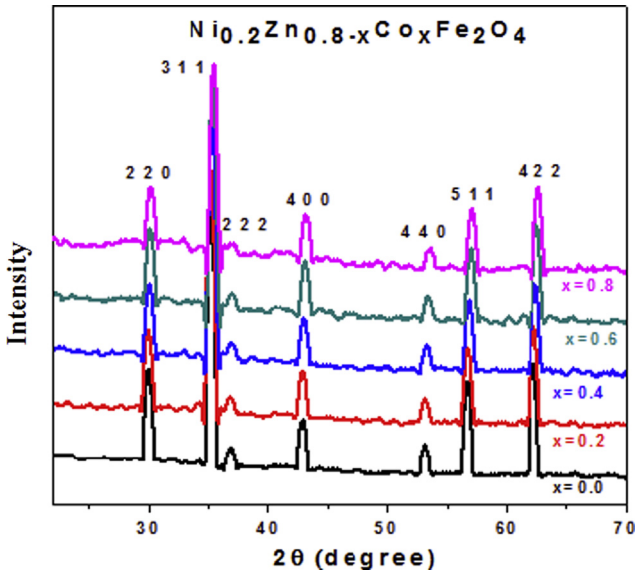

Fig. 3. Room temperature XRD patterns of NCZFO powders.

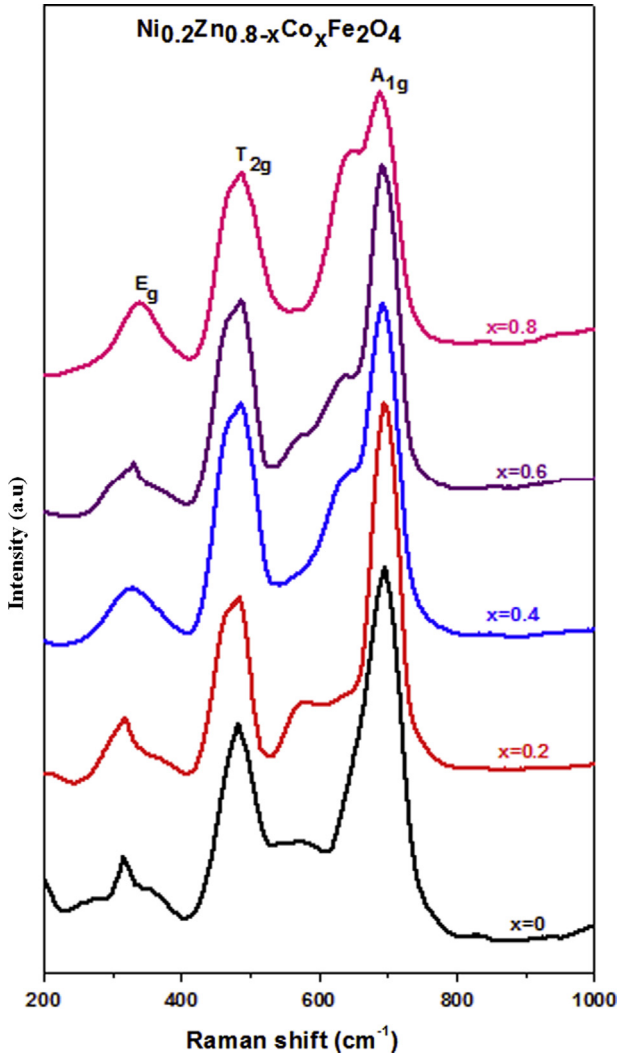

Fig. 4. Room temperature Raman spectrum of NCZFO powders.

formula [57];

$$a = \frac{\lambda}{2}\left(\frac{h^2 + k^2 + l^2}{\sin\ \theta}\right) \quad (27)$$

where ($h\ k\ l$) are the Miller indices, and θ is the diffraction angle corresponding to the ($h\ k\ l$) plane. The lattice parameter of the ferrites decreases from 0.844 nm to 0.8405 nm with increase in Co^{2+} ion content. This decrease can be attributed to the substitution of the smaller Co^{2+}(0.065 nm)ions for the larger Zn^{2+}(0.074 nm) ions [58,59]. The Scherrer's equation (Eq. (1)) is used for calculating the crystallite size by obtaining the data from the X-ray diffraction peaks [35,60] and found to be in the range of 11–8nm.

3.2. Raman spectrum study

Raman spectroscopy is a non-destructive material characterization technique and is sensitive to structural disorder. It provides an important tool to probe the surface and structural properties of materials. The Raman spectra were recorded within the frequency range 200–1000 cm^{-1} at room temperature and are shown in Fig. 4. There are three first-order Raman active modes (A_{1g}+E_g+T_{2g}), and all these modes are observed at ambient conditions. The vibration frequencies for different compositions are presented in Table 1. The A_{1g} mode is due to symmetric stretching of oxygen atoms along Fe–O bonds, E_g are due to symmetric bending of oxygen with respect to Fe and T_{2g} is due to asymmetric stretching of Fe [61]. Here, the notation A is for one dimensional representation, E for two and T for three dimensional representations, g denotes the symmetry with respect to the center of inversion [62].In the cubic spinels including ferrites, the modes at above 600 cm^{-1} mostly correspond to the motion of oxygen in tetrahedral group (A-site) [63], and the other low frequency modes represent the characteristics of the octahedral group (B-site) of ferrites [34]. The hump in the Raman spectra of around 600 cm^{-1} may be due to structural deformation resulted due to formation of Fe^{2+} ions on octahedral site [34,64].

It is know that if the unit cell volume of the compound increases the vibration frequency of Raman modes decreases [65]. Similar behavior is observed in the T_{2g} and E_g Raman modes (Table 1). However the A_{1g} mode show an increased Raman frequency of vibration. The A_{1g} mode is due to symmetric stretching of O-atoms along Fe–O bonds. The Co is a magnetic material and it occupies the space in octahedral site, whereas non-magnetic Zn is present in tetrahedral site of spinel structure. The Fe present in the octahedral site has a magnetic behavior and magnetically interact with Co. Due to these reasons, it might be possible that the intermolecular distance between Fe and O-atoms increases, so the bonding energy between them decreases resulting a Raman frequency shift towards higher side (Table 1).

3.3. Fourier transformed infrared analysis

The formation of the spinel structure is also confirmed by using the FTIR spectra, shown in Fig. 5. In ferrites the metal ions are situated in two different sub-lattices designated as tetrahedral (A-site) and octahedral (B-site) according to the geometrical configuration of the oxygen nearest neighbors. The high frequency band υ_1 is observed in the range from 576.5 to 566.7 cm^{-1}, associated A-site, whereas the low

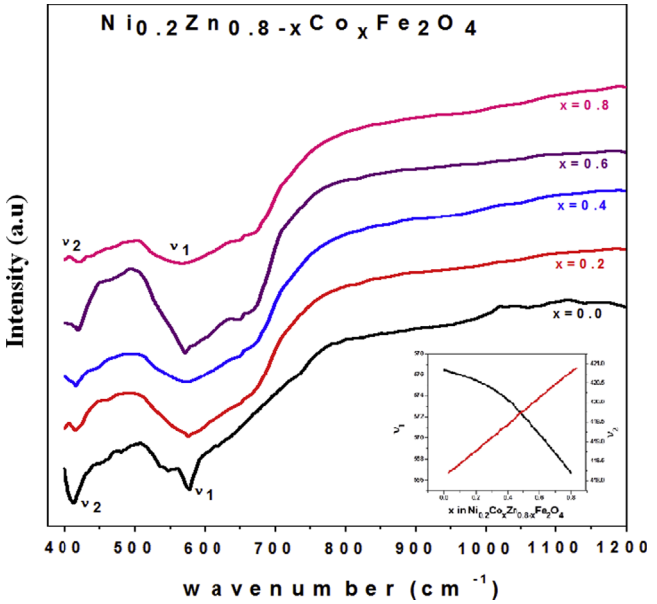

Fig. 5. Room temperature FTIR spectra of NZFO powders. The inset shows the variation of wavenumber as a function of Co-content.

Table 1
Selected peak positions of NCZFO obtained from Raman spectra and FTIR spectra.

Compositions	Raman spectra			FTIR spectra	
	Tetrahedral sites modes (cm^{-1})	Octahedral sites modes (cm^{-1})		Tetrahedral peak position (cm^{-1})	Octahedral peak position (cm^{-1})
	A_{1g}	T_{2g}	E_g		
$Ni_{0.2}Zn_{0.8}Fe_2O_4$	696.3	483.5	315.8	576.5	414.6
$Ni_{0.2}Co_{0.2}Zn_{0.6}Fe_2O_4$	695.6	485.8	320.1	575.6	415.3
$Ni_{0.2}Co_{0.4}Zn_{0.4}Fe_2O_4$	692.2	486.9	328.8	573.9	416.6
$Ni_{0.2}Co_{0.6}Zn_{0.2}Fe_2O_4$	690.6	487.8	331.9	570.4	418.2
$Ni_{0.2}Co_{0.8}Fe_2O_4$	688.7	489.5	340.2	566.7	420.9

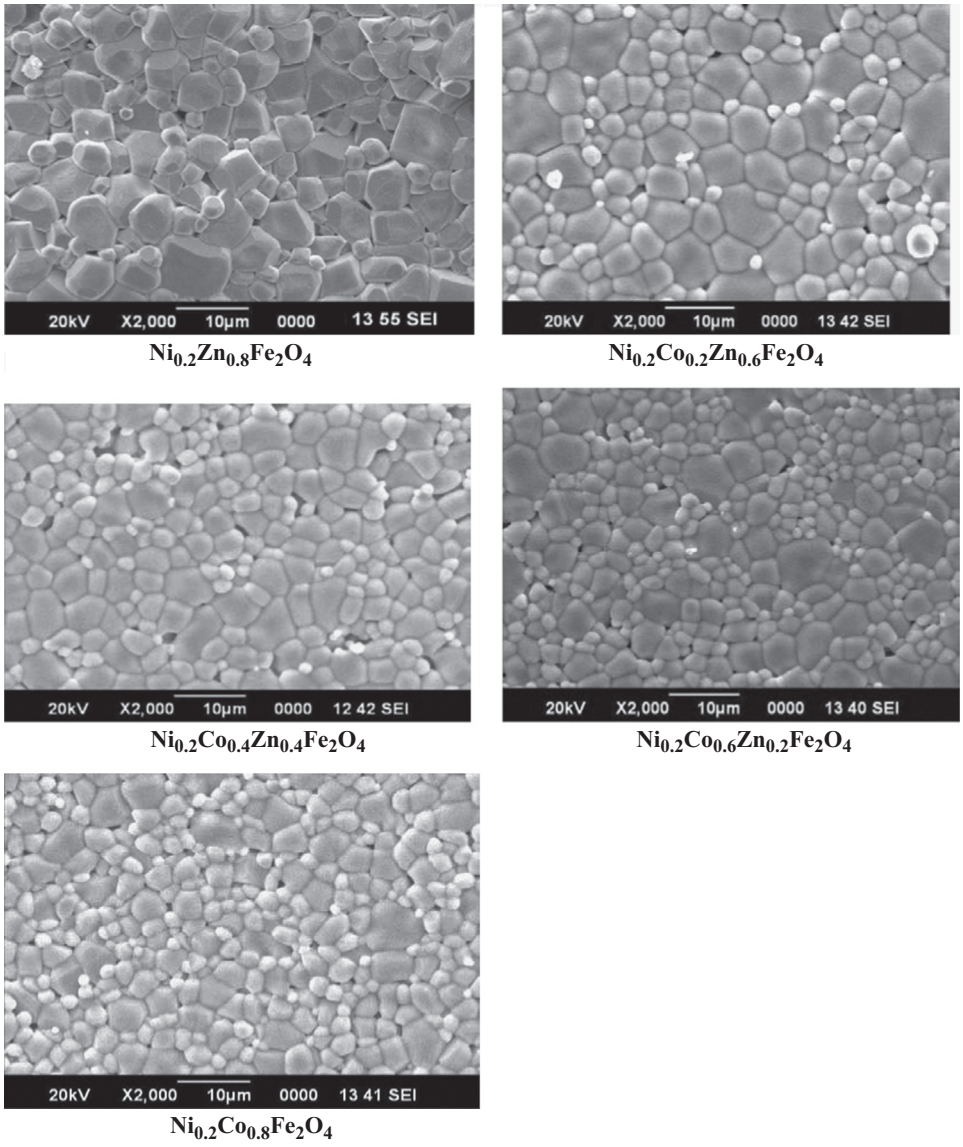

Fig. 6. Micrographs of NCZFO with 2000 × magnification and EDX spectra of corresponding composition (below).

Table 2
The bulk density, apparent porosity and microwave dielectric properties of sintered NCZFO disks.

Compositions	Density (gm/cm^3)	App. porosity (P)	ε_r^{th}	ε_r	ε_r^{corr}	tan δ	μ_r	tan δ_m	$Q \times f_r$ (GHz)	τ_f (ppm/°C)
$Ni_{0.2}Zn_{0.8}Fe_2O_4$	5.724	0.063	8.244	7.474	8.18	0.00193	2.1085	0.1029	2179.372	−75.85
$Ni_{0.2}Co_{0.2}Zn_{0.6}Fe_2O_4$	5.359	0.031	6.003	5.709	5.974	0.00226	2.8661	0.0984	1849.288	−64.15
$Ni_{0.2}Co_{0.4}Zn_{0.4}Fe_2O_4$	5.436	0.03	5.985	5.691	5.947	0.00219	2.9654	0.0975	1907.462	−47.20
$Ni_{0.2}Co_{0.6}Zn_{0.2}Fe_2O_4$	5.647	0.028	5.958	5.664	5.902	0.00207	3.0769	0.0971	2018.357	−32.36
$Ni_{0.2}Co_{0.8}Fe_2O_4$	5.604	0.034	5.887	5.548	5.831	0.00214	3.2179	0.096	1976.296	−19.32

frequency band υ_2 is observed within the frequency range 420.9–414.6 cm^{-1}associated to octahedral B-site (Table 1.). Similar vibrations are also observed by Zahi [24] at ∼570 cm^{-1}, assigned to tetrahedral bond stretching and the band at ∼418 cm^{-1}, assigned to the vibration in the octahedral site of the composition $Ni_{0.5}Zn_{0.5}Fe_2O_4$. The variation of these two band position as a function of Co-content is shown as an inset of Fig. 5. The high frequency band (υ_1) found to be shifting towards low frequency side, while low frequency band (υ_2) found shifting towards high frequency side with increases in Co-content. Waldron [66] and Hafner [67], attributed the υ_1 band to the intrinsic vibrations of the tetrahedral groups, the (υ_2) band to the octahedral groups. According to Prakash and Baijal [68] Ni^{2+} and Co^{2+} is stabilized in the octahedral

crystal field whereas Zn^{2+} prefers tetrahedral sites because of their ability to form covalent bonds involving sp^3 hybrid orbital's. The presence of lower radii Ni^{2+} and Co^{2+} in place of higher radii and higher atomic weight Zn^{2+} increases the bond length of Fe^{3+}–A site ions. This modification also reduces the bond length of Fe^{3+}–O^{2-}. Furthermore, the presence of isolated super paramagnetic clusters at B-sites screened by the diamagnetic Zn ions has been observed in Ni–Zn ferrites by Mossbauer studies [69,70]. These may be the reason for the observed change in band positions.

3.4. Scanning electron micrograph study

Fig. 6 shows the representative scanning electron micrographs of NCZFO ceramics sintered at 1200 °C. From the micrographs one can notice that grains having different dimension are homogeneously distributed. The grain size was estimated by drawing random lines of known length and counting the number of grains along each line. The average grain sizes of the sintered samples are found to be decreasing with increase in Co-content from 8 to 4 μm.

3.5. Microwave dielectric and magnetic studies

The storages capacity for the electric and magnetic energy is caused by the polarizations of electrical and magnetic dipoles. The storage capacity of ferrites increases as the value of the real part of dielectric and magnetic constant increases. The real part of permittivity ($\mathcal{E}'$), i.e., dielectric constant (ϵ_r), is directly dependent on electric polarizations [40,71]. The low dielectric constant (ϵ_r) is mainly due to the low ionic polarizability [72]. Shannon [73], suggested that molecular polarizabilities of complex substances can be broken up into the polarizabilities of constituent ions. In the case of spinel ferrite (AFe_2O_4), molecular polarizability can estimate from following equation:

$$\alpha\,(AB_2O_4) = \alpha\,(A^{2+}) + 2\alpha(Fe^{3+}) + 4\,\alpha(O^{2-}) \tag{28}$$

where α is polarizability. The dielectric constants of AFe_2O_4 compounds could be calculated with the polarizability from Shannon's suggestion and the Clausius–Mosotti relation [73].

$$\varepsilon_r^{Th.} = \frac{3V_m + 8\pi\alpha}{3V_m - 4\pi\alpha} \tag{29}$$

where V_m is molar volume. Molar volume of AFe_2O_4 was calculated with the unit cell parameters determined from the diffraction pattern. The value of the dielectric constant (ϵ_r) as per Shannon's suggestion ($\mathcal{E}_r^{Th}$) for NCZFO was calculated, with the value of polarizability of Ni^{2+}, Zn^{2+}, Co^{2+}, Fe^{3+} and O^{2-} are 1.23, 2.04, 1.65, 2.29 and 1.21, respectively[74,75]. The calculated permittivity of NCZFO compounds ($\mathcal{E}_r^{Th}$), observed permittivity (ϵ_r), corrected permittivity after porosity correction ($\mathcal{E}_r^{corr}$), dielectric loss (tan δ), magnetic loss (tan δ_m), and the value of porosity are shown in Table 2. The porosity correction was applied for observed permittivity as per the relation, $\epsilon_r^{corr.} = \epsilon_r(1 + 1.5\,P)$, where P is apparent porosity [76]. The calculated and observed permittivity after porosity correction showed good agreement. Microwave dielectric loss is mainly controlled by lattice-vibrational modes, pores, second phases, impurities, lattice defects and also by density.

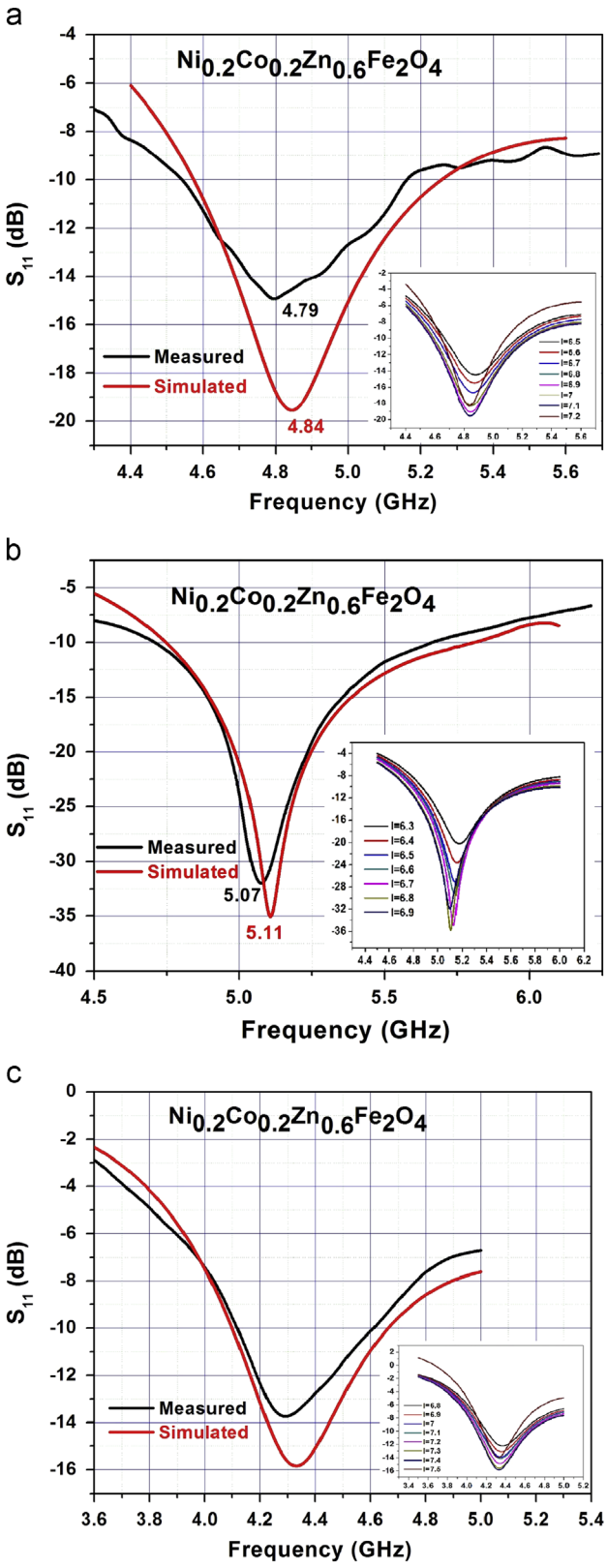

Fig. 7. Simulated and measured return loss (S_{11}) with optimum probe length for: (a) cylindrical FRA, (b) cuboid FRA and (c) triangular FRA. There inset shows the variation of simulated S_{11} for different probe lengths.

The values of permeability, and tan δ_m of NCZFO are calculated by the Nicholson–Ross–Weir conversion process. The observed dielectric and magnetic losses are lower than the same ferrites prepared by other traditional routes [77,78]. The loss parameters are directly related with the grain morphology. Also the microwave dielectric loss is also caused not only by the lattice vibrational modes but also by the pores, the second phases, the impurities, and the lattice defect [21,22]. In the present case the low losses may be due to high density of the sintered ceramics resulted from the defect free materials produced in this auto-combustion route.

It is observed that the permeability increases with increase in Co-content in NCZFO. This increase might be due to greater value of susceptibility of Cobalt than Zinc [79].The degradation of $Q \times f_r$ value can be attributed to the decrease of density resulted from the inhomogeneous grain growth as well as the evaporation of Zn [80].

Temperature co-efficient of resonant frequency, τ_f is represented by the thermal expansion coefficient, α_1 and temperature co-efficient of permittivity, τ as follows:

$$\tau_f = -\alpha_1 - \tau \tag{30}$$

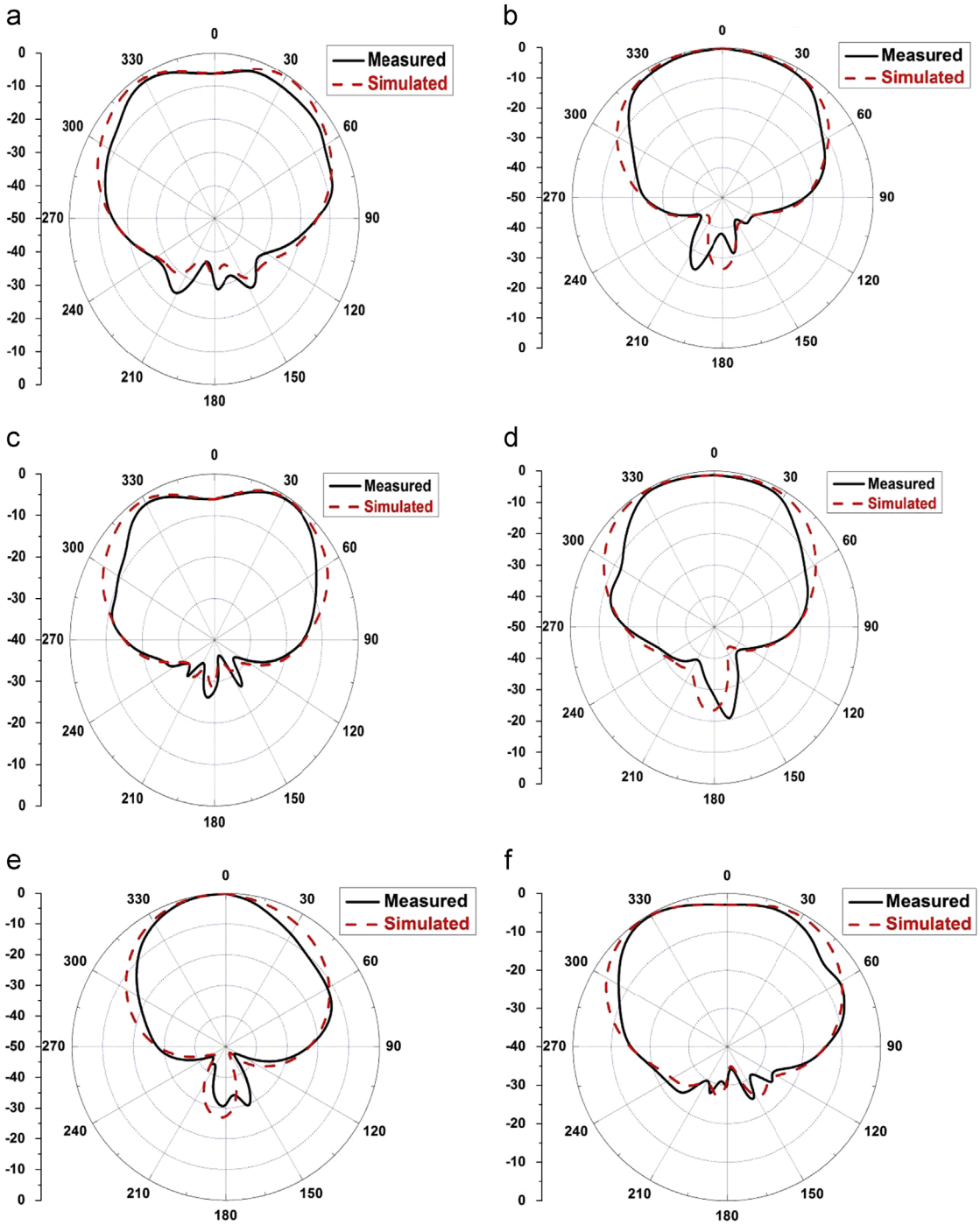

Fig. 8. Far field radiation pattern of cylindrical FRA: (a) $\varphi=0^\circ$, (b) $\varphi=90^\circ$, cuboid FRA: (c) $\varphi=0^\circ$, (d) $\varphi=90^\circ$ and triangular FRA: (e) $\varphi=0^\circ$, (f) $\varphi=90^\circ$.

The thermal expansion co-efficient of ceramic is generally in the range of 10 ppm/°C, therefore the sign and the magnitude of τ_f is depends on τ. Since the unit cell volume has strong correlation with lattice energy, τ is proportional to the relative magnitude of unit cell volume [76]. Hence, the magnitude of τ increased as the unit cell volume increased in the same structure [76], in agreement with our XRD data.

3.6. Ferrite resonator antenna study

In this section we report about the antenna behavior of cylindrical, cuboid and triangular shaped FRA prepared using $Ni_{0.2}Co_{0.2}Zn_{0.2}Fe_2O_4$ composition. The proper impedance matching between an antenna and its feed is necessary for an antenna to work efficiently. The impedance matching in an antenna is measured in terms of return loss or the scattering parameter S_{11} which represents the power reflected back into the feed (in transmitting mode). In case of probe fed FRA, S_{11} as a function of frequency is analyzed for different lengths of coaxial probe. It is observed that the coupling between the probe and FRA can be controlled by varying the probe length (l). The return loss characteristics for the FRA under consideration are shown in Fig. 7(a)–(c).The optimized impedance matching is obtained for $l=7.1$ mm, 6.8 mm and 7.4 mm for the cylindrical, cuboid and triangular FRA respectively. The parametric study of the return loss with respect to probe length l is shown in the inset of the respective Fig. 7(a)–(c).

The graphical representation of radiation properties, such as radiation intensity, field strength, radiated power, etc., as a function of spherical coordinates are shown by the radiation patterns. These properties are measured in the far field region. For an antenna with largest dimension D, the far field region is given by distance equal to or greater than $2D^2/\lambda$, where λ is wavelength. Radiation patterns are generally described in terms of E and H plane pattern.

The E-plane (or H-plane) is defined as the plane containing the electric (or magnetic) field vector and the direction of propagation. The normalized far-field radiation patterns of all different shaped FRA are shown in Fig. 8(a)–(f), respectively. The radiation characteristics show that the radiation is in broadside direction. Beam width is more in E-plane for cylindrical and cuboid compared to H-plane. However, H-plane beam width is more in triangular FRA. Further it can be observed that the maximum radiation is in the direction 35° and 33° respectively for cylindrical and cuboid FRA in E-plane and 354° in H-plane of triangular FRA. This deviation in the direction of maximum radiation from 0(360°) to 35°/33°/354° is due to the relative permeability, which is greater than unity.

The most important characteristic, which describes the performance of an antenna is gain. The gain is measured by using various techniques. The method used is two-antenna method, which utilizes two identical antennas for transmitting and receiving [81]. The gain can be calculated as

$$(G_{or})_{dB} = (G_{ot})_{dB} = \frac{1}{2}\left[20\log_{10}\left(\frac{4\pi R}{\lambda}\right) + 10\log_{10}\left(\frac{P_r}{P_t}\right)\right] \quad (31)$$

where G_{or}=gain of receiving antenna (dB), G_{ot}=gain of transmitting antenna (dB), R=antenna separation (m), λ=operating wave length (m), P_r=received power (W), P_t=transmitted power (W).

Maximum gains are measured and are tabulated in the Table 3 for different shaped FRA. It can be seen that there is an acceptable agreement between the measured and simulated results. It can be noticed that about 1 dB difference is observed between the simulated and experimental gain of the FRAs. This difference may occur due to the positioning of coaxial cable with respect to the orientation of the DRA and environmental losses. This difference is prominent in case of the triangular FRA due to its low gain suggesting the structure unsuitable for microwave antenna applications.

4. Conclusion:

$Ni_{0.2}Co_xZn_{0.8-x}Fe_2O_4$ (with $x=0$, 0.2, 0.4, 0.6 and 0.8), nanoparticles have been successfully synthesized by using the auto-combustion method. XRD study confirmed the mono-phasic cubic spinel structure of the ferrites with an average particle size ranging from 8 to 11 nm. Raman spectra show three internal vibration, symmetric and asymmetric stretching as well as symmetric bending in the materials. FT-IR spectra showed both intrinsic vibrations in tetrahedral and octahedral

Table 3
Simulated and measured antenna parameters.

	Cylindrical shaped		Cuboid shaped		Triangular shaped	
	Simulated	Measured	Simulated	Measured	Simulated	Measured
Resonant frequency (GHz)	4.84	4.79	5.11	5.07	4.33	4.29
Return loss (S11) dip (dB)	−19.7	−15.1	−35.4	−32.2	−16	−13.8
Bandwidth (GHz)	4.57–5.26	4.54–5.16	4.74–5.82	4.69–5.68	4.08–4.67	4.11–4.62
Return loss bandwidth (%)	14.26	12.94	21.14	19.53	13.63	11.89
VSWR	1.24	1.37	1.04	1.12	1.39	1.57
Gain (dB)	4.5 at 35°	3.48 at 35°	2.62 at 33°	1.79 at33°	1.97at354°	1.06 at 354°
3-dB Beam-width (HPBW)						
E-plane	107°	80°	110°	86°	60°	42°
H-plane	83°	76°	93°	67°	107°	82°

site of the structure. The vibration frequency in the octahedral site increased where as the vibration frequency in the tetrahedral site decreased with increase in Co-content. The SEM study on dense ceramics show the homogeneous distribution of different size grains and a reduction in grain size is observed with increases in Cobalt content. Dielectric constant (ϵ_r) decreased from 7.474 to 5.548 and temperature coefficient of resonant frequency (τ_f) increased from -75.85 ppm/°C to -19.32 ppm/°C respectively, and relative permeability increased from 2.1085 to 3.2179 with increase in Cobalt content. The composition $Ni_{0.2}Cu_{0.2}Zn_{0.6}Fe_2O_4$ was used to develop ferrite resonator antenna (FRA) and was studied in cylindrical, triangular and cuboid shaped with co-axial probe feeding mechanisms. The antenna characteristics have been simulated using high frequency structure simulation (HFSS) software and good agreement has been achieved between the measured and simulated results. The cuboid shaped FRA shows maximum bandwidth of 990 MHz, while the cylindrical shaped FRA shows a maximum gain of 3.48 dB respectively.

References

[1] R.C. Hansen, M. Burke, Antennas with magneto-dielectrics, Microwave and Optical Technology Letters 26 (2000) 75–78.

[2] Y. Kawano, S. Hayashida, S. Baw, Y. Koyanagi, H. Morishita, A study on miniaturization of 900 MHz and 2 GHz band antennas utilizing magnetic material, IEEE APS 3B (2005) 347–350.

[3] K.S. Min, T.V. Hong, Miniaturization of antenna using magneto-dielectric materials, IEEE APCC (2006) 1–5.

[4] S. Bae, Y. Mano, A small meander VHF and UHF antenna by magnetodielectric material, Asia-Pacific Microwave Conference (APMC), Proceedings, vol. 4, 2005, pp. 3-5.

[5] D. Souriou, J.L. Mattei, S. Boucher, A. Sharaiha, A. C. Tarot, A. Chevalier, P. Queffelec, Antenna miniaturization and nanoferrite magneto-dielectric materials, in: Proceedings of 14 International Symposium of Antenna Technology and Applied Electromagnetics [ANTEM] and the American Electromagnetics Conference [AMEREM], (2010) pp. 1–4.

[6] D. Souriou, J.L. Mattei, A. Chevalier, P. Queffelec, Influential parameters on electromagnetic properties of nickel–zinc ferrites for antenna miniaturization, Journal of Applied Physics 107 (2010) 09A518-3.

[7] H. Su, X. Tang, H. Zhang, Z. Zhong, J. Shen, Sintering dense NiZn ferrite by two-step sintering process, Journal of Applied Physics 109 (2011) 07A501-3.

[8] M.L.S. Teo, L.B. Kong, Z.W. Li, G.Q. Lin, Y.B. Gan, Development of magneto-dielectric materials based on Li-ferrite ceramics: II. DC resistivity and complex relative permittivity, Journal of Alloys and Compounds, 459, 567–575.

[9] P.I. Slick, Ferromagnetic Materials, in: E.P. Wohlfarth (Ed.), North-Holland, Amsterdam, 1980, p. 196.

[10] A.S. Albuquerque, J.D. Ardisson, W.A.A. Macedo, M.C.M. Alves, Nanosized powders of NiZn ferrite: synthesis, structure, and magnetism, Journal of Applied Physics 87 (2000) 4352–4357.

[11] K. Buell, H. Mosallaei, K. Sarabandi, A substrate for small patch antennas providing tunable miniaturization factors, IEEE Transactions on Antennasand Propagation 54 (1) (2006) 135–146.

[12] H. Su, X. Tang, H. Zhang, Y. Jing, F. Bai, Z. Zhong, Low-loss NiCuZn ferrite with matching permeability and permittivity by two-step sintering process, Journal of Applied Physics 113 (2013) 17B301-3.

[13] M.G. Naseri, E.B. Saion, M Hashim, A.H. Shaari, H.A. Ahangar, Synthesis and characterization of zinc ferrite nanoparticles by a thermal treatment method, Solid State Communications. 151 (2011) 1031–1035.

[14] R.J.Joseyphus, C.N. Chinnasamy, B. Jeyadevan, A. Kasuya, K. Shinoda, A. Narayanasamy, K. Tohji, Synthesis of ferrite nanoparticles through aqueous process for biomedical applications, in: Proceedings of 1st International Workshop on WATER DYNAMICS Tohoku University, Sendai, Japan 17–19 March (2004) pp. 51–53.

[15] Y. Todaka, M. Nakamura, S. Hattori, K Tsuchiya, M. Umemoto, Synthesis of ferrite nanoparticles by mechanochemical processing using a ball mill, Materials Transactions 44 (2003) 277–284.

[16] S. Li, L. Liu, V.T. John, C.J. O'Connor, V.G. Harris, Cobalt-ferrite nanoparticles: correlations between synthesis procedures, structural characteristics and magnetic properties, Magnetics, IEEE Transactions 37 (2001) 2350–2352.

[17] A.M. Raval, N.R. Panchal, R.B. Jotania, Structural studies of co-spinel ferrite synthesized by an auto combustion method, Journal of Analytical Techniques 1 (2010) 01–02.

[18] A. Christou, J.F Crider, The strengthening of Ti-55 at% Ni by formation of a Ti_2Ni_3 intermetallic phase, Journal of Materials Science 7 (4) (1972) 479–480.

[19] Z.A. Munir, Synthesis of high temperature materials by self-propagating combustion methods, Fenmo Yejin Jishu/Powder Metallurgy Technology 6 (1) (1988) 1–24.

[20] A. Sutka, G. Mezinskis, Sol–gel auto-combustion synthesis of spinel-type ferrite nanomaterials, Frontiers of Materials Science 6 (2012) 128–141.

[21] A.A. Thant, S. Srimala, P. Kaung, M. Itoh, O. Radzali, M.N. Ahmad Fauzi, Low temperature synthesis of $MgFe_2O_4$ soft ferrite nanocrystallites, Journal of the Australian Ceramic Society 46 (2010) 11–14.

[22] Cheng-Liang Huang, Jun-Jie Wang, Chi-Yuen Huang, Sintering behavior and microwave dielectric properties of nano alpha-alumina, Materials Letters 59 (2005) 3746–3749.

[23] Cheng-Liang Huang, Jun-Jie Wang, Chi-Yuen Huang, Microwave dielectric properties of sintered alumina using nano-scaled powders of a alumina and TiO_2, Journal of the American Ceramic Society 90 (2007) 1487–1493.

[24] S. Zahi,Synthesis, Permeability and microstructure of the optimal nickel–zinc ferrites by sol–gel route, Journal of Electromagnetic Analysis and Applications 2 (2010) 56–62.

[25] A. Goldman, Modern Ferrite Technology, Van Nostrand Reinhold, New York, 1990 (pp. 71, 162).

[26] G.R. Slemon, Magnetoelectric Devices, Wiley, New York, 1966.

[27] S.Y. Bae, H.J. Jung, C.S. Kim, Y.J. Oh, Magnetic properties of sol–gel derived Ni–Zn ferrite thin films, Journal de Physique IV: JP 8 (2) (1998) 261–264.

[28] J.S. Lee, B.I. Lee, S.K. Joo, Effects of process parameters on structure and magnetic properties of sputtered Ni–Zn ferrite thin films, IEEE Transactions on Magnetics 35 (1999) 3415–3417.

[29] Z. Qian, G. Wang, J.M. Sivertsen, J.H. Judy, Ni–Zn ferrite thin films prepared by facing target sputtering, IEEE Transactions on Magnetics 33 (1997) 3748–3750.

[30] T. Kiyomura, M. Gomi, Room-temperature epitaxial growth of Ni–Zn ferrite thin films by pulsed laser deposition in high vacuum, Japanese Journal of Applied Physics Part 2 36 (1997) L1000–L1002.

[31] A. Verma, D.C. Dube, Processing of nickel–zinc ferrites via the citrate precursor route for high-frequency applications, Journal of the American Ceramic Societ 88 (2005) 519–523.

[32] T.Y. Byun, S.C. Byeon, K.S. Hong, Factors affecting initial permeability of Co-substituted Ni–Zn–Cu ferrites, IEEE Transactions on Magnetics 35 (1999) 3445–3447.

[33] J. Smit, H.P.J. Wijn, Ferrites, John Wiley, (Eindhovan, Philips Technical Library), New York163.

[34] K. Mohit, S.K. Rout, S. Parida, G.P. Singh, S.K. Sharma, S.K. Pradhan, I.W. Kim, Structural, optical and dielectric studies of $Ni_xZn_{1-x}Fe_2O_4$ prepared by autocombustion route, Physica B 407 (2012) 935–942.

[35] B.D. Cullity, Element of X-ray Diffraction, 2nd edition, Addison-Wesley Publication Company Inc., USA, 1978.

[36] B.W. Hakki, P.D Coleman, A dielectric resonator method of measuring inductive capacities in the millimeter range, IRE Transactions on Microwave Theory and Techniques 8 (1960) 402–410.

[37] W.E. Courtney, Analysis and evaluation of a method of measuring the complex permittivity and permeability microwave insulators, IEEE Transactions on Microwave Theory and Technology 18 (1970) 476–485.

[38] L.F. Chen, C.K. Ong, C.P. Neo, V.V. Varadan, V.K. Varadan, Microwave Electronics: Measurement and Materials Characterization, 1st edition, John Wiley & Sons Ltd., England, 2004.

[39] Y. Kobayashi, S. Tanaka, Resonant Modes of a Dielectric Rod Resonator Short-Circuited at Both Ends by Parallel Conducting Plates, IEEE Transactions on Microwave Theory and Techniques 28 (1980) 1077–1085.
[40] S. Parida, S.K. Rout, V. Subramanian, P.K. Barhai, N. Gupta, V.R. Gupta, Structural microwave dielectric properties and dielectric resonator antennastudies of $Sr(Zr_xTi_{1-x})O_3$ ceramics, Journal of Alloys and Compounds 528 (2012) 126–134.
[41] S. Parida, S.K. Rout, L.S. Cavalcante, E. Sinha, M. Siu Li, V. Subramanian, N. Gupta, V.R. Gupta, J.A. Varela, E. Longo, Structural refinement, optical and microwave dielectric properties of $BaZrO_3$, Ceramics International. 38 (2012) 2129–2138.
[42] M.L. Moreira, P.G.C. Buzolin, V.M. Longo, N.H. Nicoleti, J.R. Sambrano, M.S. Li, J.A. Varela, E. Longo, Joint experimental and theoretical analysis of order–disorder effects in cubic $BaZrO_3$ assembled nanoparticles under decaoctahedral shape, Journal of Physical Chemistry A 115 (2011) 4482–4490.
[43] Y. Kobayashi, M. Katoh,Microwave, Measurement of dielectric properties of low-loss materials by the dielectric rod resonator method, IEEE Transactions on Microwave Theory and Techniques 33 (1985) 586–592.
[44] L.F. Chen, C.K. Ong, C.P. Neo, V.V. Varadan, V.K. Varadan, Microwave Electronics: Measurement and Materials Characterization, 1st edition, John Wiley & Sons Ltd., England, 2004.
[45] A.L. de Paula, M.C. Rezende, J.J. Barroso, Experimental measurements and numerical simulation of permittivity and permeability of Teflon in X band, Journal of Aerospace Technology and Management, São José dos Campos 3 (2011) 59–64.
[46] D. Kajfez, P. Guillon, Dielectric Resonators, The Artech House Microwave Library, Norwood, MA, 1986.
[47] K.M. Luk, K.W. Leung, Dielectric Resonator Antennas, Research Studies Press Ltd, Baldock, England, 2002.
[48] P.B.A. Fechine, R.S.T. Moretzsohn, R.C.S. Costa, J. Derov, J.W. Stewart, A.J. Drehman, C. Junqueira, A.S.B. Sombra, Magneto-dielectric properties of the $Y_3Fe_5O_{12}$ and $Gd_3Fe_5O_{12}$ dielectric ferrite resonator antennas, Microwave and Optical Technology Letters 50 (2008) 2852–2857.
[49] A. Petosa, A. Ittipiboon, Y.M.M. Antar, D. Roscoe, Recent advances in dielectric-resonator antenna technology, IEEE Antennas and Propagation Magazine 40 (1998) 35–48.
[50] G.P. Junker, A.W. Glisson, A.A. Kishk, Input impedance of dielectric resonator antennas top loaded with high permittivity and conducting disks, Microwave and Optical Technology Letters 9 (1995) 204–207.
[51] G.P. Junker, A.A. Kishk, A.W. Glisson, D. Kajfez, Effect of an air gap around the coaxial probe exciting a cylindrical dielectric resonator antenna, Electronics Letters 30 (1994) 177–178.
[52] R.K. Mongia, A. Ittipiboon, Theoretical and experimental investigations on rectangular dielectric resonator antennas, IEEE Transactions on Antennas and Propagation 45 (1997) 1348–1356.
[53] Z. Peng, H. Wang, X. Yao, Dielectric resonator antennas using high permittivity ceramics, Ceramics International 30 (2004) 1211–1214.
[54] K.M. Luk, K.W. Leung, Dielectric Resonator Antennas, Hertfordshire, U.K.: Research Studies Press Ltd. (2002).
[55] R. Kumari, K. Parmar,S.K. Behera, Conformal patch fed stacked triangular dielectric resonator antenna for WLAN applications, in: Proceedings of IEEE International Conference on Emerging Trends in Robotics and Communication Technologies Sathyabama University, Chennai, Dec.03–05(2010) pp. 104–107.
[56] R. Grabovickic, Accurate calculations of geometrical factors of Hakki–Coleman shielded dielectric resonators, IEEE Transactions on Applied Superconductivity 9 (1999) 4607–4612.
[57] C.C. Hwang, J.S. Tsai, T.H. Huang, Combustion synthesis of Ni–Zn ferrite by using glycine and metal nitrates—investigations of precursor homogeneity, product reproducibility, and reaction mechanism, Materials Chemistry and Physic 93 (2005) 330–336.
[58] K. Kugimiya, H. Steinfink, Influence of crystal radii and electronegativities on the crystallization of $AB2\times4$ stoichiometries, Journal of Inorganic Chemistry 7 (1968) 1762–1770.
[59] K.B. Modi, P.V. Tanna, S.S. Laghate, H.H Joshi, The effect of Zn^{+2} substitution on some structural properties of $CuFeCrO_4$ system, Journal of Materials Science Letters 19 (2000) 1111–1113.
[60] P. Scherrer, G. Nachricht, Bestimmung der Grösse und der inneren Struktur von Kolloidteilchen mittels Röntgenstrahlen, Nachrichten von der Gesellschaft der Wissenschaften, Göttingen, Mathematisch-PhysikalischeKlasse 2 (1918) 98–100.
[61] O.N. Shebanova, P. Lazer,Raman, spectroscopic study of magnetite ($FeFe_2O_4$): a new assignment for the vibrational spectrum, Journal of Solid State Chemistry 174 (2003) 424–430.
[62] E. Prince, Mathematical Technique in Crystallography and Material Science, Springer Verlag, New York, Heidelberg, Berlin, 1982.
[63] Z. Wang, D. Schiferl, Y. Zhao, H. St., C. O'Neill, High pressure Raman spectroscopy of spinel-type ferrite $ZnFe_2O_4$, Journal of Physics and Chemistry of Solids 64 (2003) 2517–2523.
[64] G. Sathishkumar, C. Venkataraju, K. Sivakumar, Synthesis, structural and dielectric studies of nickel substituted cobalt–zinc ferrite, Materials Sciences and Applications 1 (2010) 19–24.
[65] E.S. Kim, C.J. Jeon, Microwave dielectric properties of $ATiO_3$ (A=Ni, Mg, Co, Mn) ceramics, Journal of the European Ceramic Society 30 (2010) 341–346.
[66] R.D. Waldron, Infrared spectra of ferrites, Physical Review 99 (1955) 1727–1735.
[67] S. Hafner, Ordnung/Unordnung und Ultrarotabsorption IV, Die Absorption Einiger Metalloxyde mit Spinellstruktur, Z. Kristallogr 115 (1961) 331–358.
[68] C. Prakash, J.S. Baijal,Mössbauer, studies on hyperfine field measurement in titanium doped nickel-zinc ferrites, Solid State Communications 50 (1984) 557–559.
[69] N.L. Pakhomova, V.N. Belogurov, V.A. Bylinkin, A.M. Vinnik, L. M. Kassimenko, P.E. Senkov, Low-temperature transitions and spin configurations in nickel–zinc ferrite spinels, Soviet Physics—Solid State 19 (1977) 1060–1064.
[70] R.K. Puri, U. Varshney, Mössbauer study of Zn^{2+} and Sn^{4+} additives in Nickel ferrites, Journal of Physics and Chemistry of Solids 44 (1983) 655–661.
[71] T. Tsurumi, T. Teranishi, S. Wada, H. Kakemoto, M. Nakada, J. Akedo, , 2006, Proceedings of 15th IEEE International Symposium on the Applications of ferroelectrics, isaf'06. USA (2006) pp. 1–8.
[72] C.T. Lee, C.T. Chen, C.Y. Huang, C.J. Wang,Microwave, Dielectric properties of $(Ba_{1-x}Mg_x)_5Nb_4O_{15}$ ceramics, Japanese Journal of Applied Physics 47 (2008) 4634–4637.
[73] R.D. Shannon, Dielectric polarizabilities of ions in oxides and fluorides, Journal of Applied Physics 73 (1993) 348–366.
[74] M.T. Sebastian, Dielectric Materials for Wireless Communication, 1st edition, Elsevier Publication, UK, 2008.
[75] N.W. Grimes, R.W. Grimes, Dielectric polarizability of ions and the corresponding effective number of electrons, Journal of Physics: Condensed Matter 10 (1998) 3029–3034.
[76] S.H. Yoon, D.W. Kim, S.Y. Cho, K.S. Hong, Investigation of the relations between structure and microwave dielectric properties of divalent metal tungstate compounds, Journal of the European Ceramic Society 26 (2006) 2051–2054.
[77] Shen Xiang, Wang Yan-xin, Yang Xiang, Xia Yong, Zhuang Jian-feng, Tang Pei-duo, Megahertz magneto-dielectric properties of nanosized NiZnCo ferrite from CTAB-assisted hydrothermal process, Transactions of Nonferrous Metals Society of China 19 (2009) 1588–1592.
[78] Xiang Shen, Rongzhou Gong, Zekun Feng, Yan Nie, Effective permeability of NiZnCo ferrite granular thin films, Journal of the American Ceramic Society 90 (2007) 2196–2199.
[79] J.F. Schenck, The role of magnetic susceptibility in magnetic resonance imaging: MRI magnetic compatibility of the first and second kind, General Electric Corporate Research and Development Center, Schenectady, New York, Medical Physics 23 (1996) 815–851.
[80] S.S. Rajput, S. Keshri, V.R. Gupta, Microwave dielectric properties of $(1-x)Mg_{0.95}Zn_{0.05}TiO_3$–$(x)Ca_{0.6}La_{0.8/3}TiO_3$ceramic composites, Journal of Alloys and Compounds 552 (2013) 219–226.
[81] C.A. Balanis, Antenna Theory Analysis and Design, 3rd edition, John Wiley & Sons, Inc., Publication, USA, 2005.